

Search for effective Lorentz and CPT violation using ZEUS data

ZEUS Collaboration

Abstract

Lorentz and CPT symmetry in the quark sector of the Standard Model are studied in the context of an effective field theory using ZEUS $e^\pm p$ data. Symmetry-violating effects can lead to time-dependent oscillations of otherwise time-independent observables, including scattering cross sections. An analysis using five years of inclusive neutral-current deep inelastic scattering events corresponding to an integrated HERA luminosity of 372 pb^{-1} at $\sqrt{s} = 318 \text{ GeV}$ has been performed. No evidence for oscillations in sidereal time has been observed within statistical and systematic uncertainties. Constraints, most for the first time, are placed on 42 coefficients parameterising dominant CPT-even dimension-four and CPT-odd dimension-five spin-independent modifications to the propagation and interaction of light quarks.

The ZEUS Collaboration

I. Abt¹, R. Aggarwal², V. Aushev³, O. Behnke⁴, A. Bertolin⁵, I. Bloch⁶, I. Brock⁷,
N.H. Brook^{8,a}, R. Brugnera⁹, A. Bruni¹⁰, P.J. Bussey¹¹, A. Caldwell¹, C.D. Catterall¹²,
J. Chwastowski¹³, J. Ciborowski^{14,b}, R. Ciesielski^{4,c}, A.M. Cooper-Sarkar¹⁵, M. Corradi^{10,d},
R.K. Dementiev¹⁶, S. Dusini⁵, J. Ferrando⁴, B. Foster^{15,e}, E. Gallo^{17,f}, D. Gangadharan^{18,g},
A. Garfagnini⁹, A. Geiser⁴, G. Grzelak¹⁴, C. Gwenlan¹⁵, D. Hochman¹⁹, N.Z. Jomhari⁴,
I. Kadenko³, U. Karshon¹⁹, P. Kaur²⁰, R. Klanner¹⁷, I.A. Korzhavina¹⁶, N. Kovalchuk¹⁷,
M. Kuze²¹, B.B. Levchenko¹⁶, A. Levy²², B. Löhner⁴, E. Lohrmann¹⁷, A. Longhin⁹,
F. Lorkowski⁴, E. Lunghi²³, I. Makarenko⁴, J. Malka^{4,h}, S. Masciocchi^{24,i}, K. Nagano²⁵,
J.D. Nam²⁶, Yu. Onishchuk³, E. Paul⁷, I. Pidhurskyi²⁷, A. Polini¹⁰, M. Przybycień²⁸,
A. Quintero²⁵, M. Ruspa²⁹, U. Schneekloth⁴, T. Schörner-Sadenius⁴, I. Selyuzhenkov²⁴,
M. Shchedrolosiev⁴, L.M. Shcheglova¹⁶, N. Sherrill³⁰, I.O. Skillicorn¹¹, W. Słomiński³¹,
A. Solano³², L. Stanco⁵, N. Stefaniuk⁴, B. Surrow²⁶, K. Tokushuku²⁵, O. Turkot^{4,h},
T. Tymieniecka³³, A. Verbytskyi¹, W.A.T. Wan Abdullah³⁴, K. Wichmann⁴, M. Wing^{8,j},
S. Yamada²⁵, Y. Yamazaki³⁵, A.F. Żarnecki¹⁴, O. Zenaiev^{4,k}

- 1 *Max-Planck-Institut für Physik, München, Germany*
- 2 *DST-Inspire Faculty, Department of Technology, SPPU, India*
- 3 *Department of Nuclear Physics, National Taras Shevchenko University of Kyiv, Kyiv, Ukraine*
- 4 *Deutsches Elektronen-Synchrotron DESY, Notkestr. 85, 22607 Hamburg, Germany*
- 5 *INFN Padova, Padova, Italy*^A
- 6 *Deutsches Elektronen-Synchrotron DESY, Platanenallee 6, 15738 Zeuthen, Germany*
- 7 *Physikalisches Institut der Universität Bonn, Bonn, Germany*^B
- 8 *Physics and Astronomy Department, University College London, London, United Kingdom*^C
- 9 *Dipartimento di Fisica e Astronomia dell'Università and INFN, Padova, Italy*^A
- 10 *INFN Bologna, Bologna, Italy*^A
- 11 *School of Physics and Astronomy, University of Glasgow, Glasgow, United Kingdom*^C
- 12 *Department of Physics, York University, Ontario, Canada M3J 1P3*^D
- 13 *The Henryk Niewodniczanski Institute of Nuclear Physics, Polish Academy of Sciences, Krakow, Poland*
- 14 *Faculty of Physics, University of Warsaw, Warsaw, Poland*
- 15 *Department of Physics, University of Oxford, Oxford, United Kingdom*^C
- 16 *Affiliated with an institute covered by a current or former collaboration agreement with DESY*
- 17 *Hamburg University, Institute of Experimental Physics, Hamburg, Germany*^E
- 18 *Physikalisches Institut of the University of Heidelberg, Heidelberg, Germany*
- 19 *Department of Particle Physics and Astrophysics, Weizmann Institute, Rehovot, Israel*
- 20 *Sant Longowal Institute of Engineering and Technology, Longowal, Punjab, India*
- 21 *Department of Physics, Tokyo Institute of Technology, Tokyo, Japan*^F
- 22 *Raymond and Beverly Sackler Faculty of Exact Sciences, School of Physics, Tel Aviv University, Tel Aviv, Israel*^G
- 23 *Department of Physics, Indiana University Bloomington, Bloomington, IN 47405, USA*
- 24 *GSI Helmholtzzentrum für Schwerionenforschung GmbH, Darmstadt, Germany*
- 25 *Institute of Particle and Nuclear Studies, KEK, Tsukuba, Japan*^F
- 26 *Department of Physics, Temple University, Philadelphia, PA 19122, USA*^H
- 27 *Institut für Kernphysik, Goethe Universität, Frankfurt am Main, Germany*
- 28 *AGH University of Science and Technology, Faculty of Physics and Applied Computer Science, Krakow, Poland*
- 29 *Università del Piemonte Orientale, Novara, and INFN, Torino, Italy*^A

- ³⁰ *Department of Physics and Astronomy, University of Sussex, Brighton, BN1 9QH, United Kingdom*^I
- ³¹ *Department of Physics, Jagellonian University, Krakow, Poland*^J
- ³² *Università di Torino and INFN, Torino, Italy*^A
- ³³ *National Centre for Nuclear Research, Warsaw, Poland*
- ³⁴ *National Centre for Particle Physics, Universiti Malaya, 50603 Kuala Lumpur, Malaysia*^K
- ³⁵ *Department of Physics, Kobe University, Kobe, Japan*^F

^A supported by the Italian National Institute for Nuclear Physics (INFN)

^B supported by the German Federal Ministry for Education and Research (BMBF), under contract No. 05 H09PDF

^C supported by the Science and Technology Facilities Council, UK

^D supported by the Natural Sciences and Engineering Research Council of Canada (NSERC)

^E supported by the German Federal Ministry for Education and Research (BMBF), under contract No. 05h09GUF, and the SFB 676 of the Deutsche Forschungsgemeinschaft (DFG)

^F supported by the Japanese Ministry of Education, Culture, Sports, Science and Technology (MEXT) and its grants for Scientific Research

^G supported by the Israel Science Foundation

^H supported in part by the Office of Nuclear Physics within the U.S. DOE Office of Science

^I supported in part by the Science and Technology Facilities Council grant number ST/T006048/1

^J supported by the Polish National Science Centre (NCN) grant no. DEC-2014/13/B/ST2/02486

^K supported by HIR grant UM.C/625/1/HIR/149 and UMRG grants RU006-2013, RP012A-13AFR and RP012B-13AFR from Universiti Malaya, and ERGS grant ER004-2012A from the Ministry of Education, Malaysia

- a* now at University of Bath, United Kingdom
- b* also at Lodz University, Poland
- c* now at Rockefeller University, New York, NY 10065, USA
- d* now at INFN Roma, Italy
- e* also at DESY and University of Hamburg, Hamburg, Germany and supported by a Leverhulme Trust Emeritus Fellowship
- f* also at DESY, Hamburg, Germany
- g* now at University of Houston, Houston, TX 77004, USA
- h* now at European X-ray Free-Electron Laser facility GmbH, Hamburg, Germany
- i* also at Physikalisches Institut of the University of Heidelberg, Heidelberg, Germany
- j* also supported by DESY, Hamburg, Germany
- k* now at Hamburg University, II. Institute for Theoretical Physics, Hamburg, Germany

1 Introduction

Relativity is one of the best established principles in physics. It concerns the invariance of physical laws under transformations of spacetime orientation including spatial rotations and velocity boosts. As a core principle of classical and modern theories, relativity implies that identical measurements performed with different spacetime orientations observe the same laws of motion, with their respective results linked by the appropriate transformation. In general, any theory exhibiting isotropy under rotations and relativistic boosts is said to be Lorentz invariant.

Searches for violations of isotropy date back to the Michelson–Morley experiment, which attempted to measure the rotational anisotropy of light propagation [1]. Its null result heavily influenced the support of special relativity. As rotations and boosts do not commute, the violation of rotation invariance implies the violation of boost invariance and vice versa. However, experimental indications of such symmetry violations do not necessarily imply Lorentz violation in an underlying fundamental theory. This can be seen, for example, by considering the Earth’s motion in the presence of a hypothetical Lorentz-invariant background field, perhaps representing a galactic dark-matter halo. If the field’s velocity distribution is isotropic in the galactic frame as is commonly assumed, it will be anisotropic in an Earth-based laboratory frame, leading to locally time-dependent observations primarily as a function of the Earth’s annual revolution around the Sun and its axial rotation. Lorentz violation implies CPT violation in many theoretical frameworks. Generic searches for violations of rotation invariance encompass a wide range of possible physical effects.

Model-independent experimental tests of Lorentz invariance and related fundamental symmetries have been intensively performed for over two decades, with no significant deviations observed [2]. In spite of the substantial progress achieved in understanding possible Lorentz and CPT violation, relatively few studies involving the quark sector directly have been performed, leaving unexamined a vast array of potential signals. One reason for this stems from the difficulty in interpreting quark-level interactions in stable-hadron and lepton processes. A few previous collider-based searches have resulted in constraints on renormalisable and rotationally invariant quark-sector effects in the final states of e^+e^- collisions using LEP data [3] and on top-quark effects [4] using Tevatron data [5]. Studies of Lorentz-violating effects in hadronic processes have recently been addressed in a series of theoretical studies on DIS [6–8] and the Drell–Yan process [9, 10].

This paper describes a search for effective rotation-violating signals affecting light quarks ($f = u, d, s$) performed with $e^\pm p$ data collected by the ZEUS detector at HERA. Deep inelastic scattering (DIS) is chosen as a suitable test process because of its strong theoretical foundation and the wealth of available data. To remain model independent, the technical framework employed is rooted in an effective field theory (EFT) [11] and is reviewed in the following section. Modified DIS cross sections and related observables incorporating the

effects of interest are then described, followed by the experimental setup, analysis method and associated Monte Carlo studies, and a description of systematic uncertainties. Constraints on effective couplings parameterising signals that violate rotational symmetry in light-quark interactions are given.

2 Theory

2.1 The Standard Model Extension

Searches for Lorentz-violating effects often make use of the comprehensive EFT framework known as the Standard Model Extension (SME) [12–15]. In the absence of general-relativistic effects, the SME action may be written as

$$S_{\text{SME}} = S_{\text{SM}} + S_{\text{LV}}, \quad (1)$$

where S_{SM} is the action of the Standard Model and S_{LV} represents all possible Lorentz-violating terms constructed from additional interactions of Standard Model fields. These terms are typically treated as perturbations with respect to conventional effects. The analysis presented here is restricted to selected dimension-four and -five operators. As CPT violation implies Lorentz violation in a unitary and local quantum field theory [12,16], CPT-violating operators are also contained in the SME. Further information on the SME can be found in, e.g., accessible reviews [17,18].

The dimension-four operators, $\bar{\psi}_f \gamma_\mu i D_\nu \psi_f$, considered here are the dominant spin-independent and renormalisable quark-sector modifications of quantum electrodynamics [6]¹,

$$\mathcal{L}_c = \frac{1}{2} \sum_f c_f^{\mu\nu} \bar{\psi}_f \gamma_\mu i D_\nu \psi_f + \text{h.c.}, \quad (2)$$

where $D_\nu = \partial_\nu + i e e_f A_\nu$, e is the electron charge, e_f are the relative quark charges and A_ν is the photon field. The coefficients $c_f^{\mu\nu}$ control the magnitude of Lorentz-violating effects. Since the coefficient and operator Lorentz indices in Eq. (2) are contracted, \mathcal{L}_c is invariant under coordinate transformations, known as "observer transformations" [12]. Accordingly, observer transformations have no sensitivity to anisotropies parameterised by $c_f^{\mu\nu}$. If instead a "particle transformation" is performed, the particle fields ψ_f, A_ν, \dots are transformed while the coordinates are unaffected. This could be realised, for example, by physically rotating the system described by the particle fields. In this case, \mathcal{L}_c is not Lorentz invariant in general. This occurs because $c_f^{\mu\nu}$ is invariant under particle transformations, whereas the system described by the particle fields is not. A distinction between transforming the system as opposed to transforming the observer is present. This violates

¹ The notation h.c. is an abbreviation for Hermitian conjugation.

Lorentz invariance. These c -type coefficients may be taken as symmetric and traceless, leaving nine observable coefficients per flavour f [13].

All gauge-invariant effects in the minimal and non-minimal sector of non-Abelian gauge theories were classified and dimension-five, spin-independent, and CPT-violating effects

$$\mathcal{L}_{a^{(5)}} = -\frac{1}{2} \sum_f a_f^{(5)\mu\alpha\beta} \bar{\psi}_f \gamma_\mu i D_{(\alpha} i D_{\beta)} \psi_f + \text{h.c.} , \quad (3)$$

parameterised by the $a^{(5)}$ -type coefficients $a_f^{(5)\mu\alpha\beta}$, were considered for DIS [8]. Note that $\mathcal{L}_{a^{(5)}}$ represents the dominant non-minimal and spin-independent CPT-violating effects on quarks, and the parenthesis notation denotes symmetrisation with respect to the indices α, β . Similar to the case of the c -type coefficients, the $a^{(5)}$ -type coefficients may be taken to be totally symmetric and traceless [9, 19, 20]. This subset of coefficients is denoted $a_{Sf}^{(5)\mu\alpha\beta}$ and contains 16 independent observable components per flavour.

Simulations have been performed assessing the sensitivity of the c -type and $a^{(5)}$ -type coefficients for quarks and antiquarks as measured in DIS data from HERA [21], Electron–Ion Collider pseudodata [7], and in the Drell–Yan process using LHC data [22].

2.2 Adding SME effects to the description of DIS

The class of operators that modify the free propagation of quarks and their covariant couplings to gauge fields was examined [9], resulting in the development of a tree-level, Lorentz-violating version of the parton model. This leads to a modified description of DIS.

In the following, the external momenta of the incident lepton and proton are denoted by l^μ and p^μ , respectively, while the scattered lepton and exchanged momentum are denoted by l'^μ and $q^\mu = l^\mu - l'^\mu$, where $-q^2 \equiv Q^2$ is the momentum transfer. The Bjorken variables are

$$x_{\text{Bj}} = \frac{Q^2}{2p \cdot q} , \quad y_{\text{Bj}} = \frac{p \cdot q}{p \cdot l} , \quad (4)$$

where $s \approx 2p \cdot l$ and $Q^2 \approx x_{\text{Bj}} y_{\text{Bj}} s$. In the DIS limit, and working at zeroth order in the strong coupling constant, the inclusion of Lorentz-violating effects described by Eq. (2) at tree level results in the cross section²

$$\frac{d\sigma}{dx_{\text{Bj}} dy_{\text{Bj}} d\varphi} = \frac{\alpha^2 y_{\text{Bj}}}{2Q^4} \sum_f e_f^2 \frac{1}{\tilde{Q}_f^2} L_{\mu\nu} H_f^{\mu\nu} f_f(\tilde{x}_f) , \quad (5)$$

where φ is the scattered lepton azimuthal angle, $\tilde{Q}_f^2 = -\tilde{q}_f^2 = -(q^\mu + c_f^{\mu q})(q_\mu + c_{f\mu q})$ where

² Equation (5) reduces to the leading-order Standard Model cross section in the limit $c_f^{\mu\nu} \rightarrow 0$.

$c_f^{\mu q} \equiv c_f^{\mu\nu} q_\nu$, and

$$L_{\mu\nu} H_f^{\mu\nu} = 8 \left[2(\widehat{k}_f \cdot l)(\widehat{k}_f \cdot l') + \widehat{k}_f \cdot (l - l')(l \cdot l') + 2(\widehat{k}_f \cdot l) \left(c_f^{\widehat{k}_f l'} + c_f^{l' \widehat{k}_f} - c_f^{l' l'} \right) \right. \\ \left. + 2(\widehat{k}_f \cdot l') \left(c_f^{\widehat{k}_f l} + c_f^{l \widehat{k}_f} + c_f^{ll} \right) - 2(l \cdot l') c_f^{\widehat{k}_f \widehat{k}_f} \right], \quad (6)$$

with $\widehat{k}_f^\mu = \tilde{x}_f(p^\mu - c_f^{\mu p})$. The parton distribution functions (PDFs) are denoted $f_f(\tilde{x}_f)$ and are evaluated at the shifted Bjorken variable [9]

$$\tilde{x}_f = x_{\text{Bj}} \left(1 + \frac{2c_f^{qq}}{q^2} \right) + \frac{x_{\text{Bj}}^2}{q^2} (c_f^{pq} + c_f^{qp}), \quad (7)$$

where $c_f^{qq} \equiv c_f^{\mu\nu} q_\mu q_\nu$, etc. The PDFs are taken to be the conventional leading-order Standard Model PDFs evaluated at \tilde{x}_f using the MSTW 2008 variable-flavour PDF set [23], as implemented in the program ManeParse [24, 25].³ Note that since the c -type coefficients control CPT-even effects, the quark and antiquark contributions are identical in the cross section Eq. (5), except for the PDF dependence. Thus, for these coefficients, $d\sigma \propto (f_f + f_{\bar{f}})$ and the dominant sensitivity is expected at low x_{Bj} .

The cross section including effects of the $a^{(5)}$ -type coefficients from Eq. (3) is [6, 9]

$$\frac{d\sigma}{dx_{\text{Bj}} dy_{\text{Bj}} d\varphi} = \frac{\alpha^2}{Q^4} \sum_f F_{2f} \left[\frac{y_{\text{Bj}} s^2}{\pi} [1 + (1 - y_{\text{Bj}})^2] \delta_{\text{S}f} + \frac{y_{\text{Bj}}(y_{\text{Bj}} - 2)s}{x_{\text{Bj}}} x_{\text{S}f} \right. \\ \left. - \frac{4}{x_{\text{Bj}}} \left(4x_{\text{Bj}}^2 a_{\text{S}f}^{(5)ppl} + 6x_{\text{Bj}} a_{\text{S}f}^{(5)lpq} + 2a_{\text{S}f}^{(5)lqq} \right) \right. \\ \left. + 2y_{\text{Bj}} \left(4x_{\text{Bj}}^2 a_{\text{S}f}^{(5)ppp} + 4x_{\text{Bj}} a_{\text{S}f}^{(5)ppq} + 4x_{\text{Bj}} a_{\text{S}f}^{(5)lpp} + 2a_{\text{S}f}^{(5)lpq} + a_{\text{S}f}^{(5)pqq} \right) \right. \\ \left. + \frac{4y_{\text{Bj}}}{x_{\text{Bj}}} \left(2x_{\text{Bj}} a_{\text{S}f}^{(5)llp} + a_{\text{S}f}^{(5)llq} \right) \right], \quad (8)$$

where $F_{2f} = e_f^2 f_f(x'_{\text{S}f}) x'_{\text{S}f}$ with $x'_{\text{S}f} = x_{\text{Bj}} - x_{\text{S}f}$ and

$$\delta_{\text{S}f} = \frac{\pi}{y_{\text{Bj}} s} \left[1 + \frac{2}{y_{\text{Bj}} s} \left(4x_{\text{Bj}} a_{\text{S}f}^{(5)ppq} + 3a_{\text{S}f}^{(5)pqq} \right) \right], \quad (9)$$

$$x_{\text{S}f} = -\frac{2}{y_{\text{Bj}} s} \left(2x_{\text{Bj}}^2 a_{\text{S}f}^{(5)ppq} + 3x_{\text{Bj}} a_{\text{S}f}^{(5)pqq} + a_{\text{S}f}^{(5)qqq} \right), \quad (10)$$

$$a_{\text{S}f}^{(5)\mu\alpha\beta} = \frac{1}{3} \sum_{(\mu\alpha\beta)} \left(a_f^{(5)\mu\alpha\beta} - \frac{1}{6} a_f^{(5)\mu\rho\sigma} \eta_{\rho\sigma} \eta^{\alpha\beta} - \frac{1}{3} a_f^{(5)\rho\mu\sigma} \eta_{\rho\sigma} \eta^{\alpha\beta} \right), \quad (11)$$

where $a_{\text{S}f}^{(5)qqq} \equiv a_{\text{S}f}^{(5)\mu\alpha\beta} q_\mu q_\alpha q_\beta$, etc. The sum in Eq. (11) denotes symmetrisation with respect to the indices μ, α and β , and $\eta_{\rho\sigma}$ is the Minkowski metric. As the operator in Eq. (3) is odd under a CPT transformation, for the antiparticle contributions to the sum

³ It was checked that effects of a variation of the input PDF set are negligible. Potential effects from Lorentz violation on the PDF starting scale parametrization and on the PDF evolution were neglected.

in Eq. (8), a replacement $a_{Sf}^{(5)\mu\alpha\beta} \rightarrow -a_{Sf}^{(5)\mu\alpha\beta}$ for antiquark flavours must be performed, along with multiplication of the appropriate PDFs. In contrast to the c -type coefficients, this feature implies $d\sigma \propto (f_f - f_{\bar{f}})$, thus giving weaker sensitivity at low x_{Bj} . A depiction of the DIS process with Lorentz violation is shown in Fig. 1.

2.3 Sidereal signals

An experiment is sensitive to the c - and $a^{(5)}$ -type coefficients as they appear in the laboratory frame. The cross sections Eqs. (5) and (8) therefore must be evaluated in the laboratory frame of the ZEUS detector. This frame is non-inertial due to the Earth's axial rotation and revolution around the Sun. By convention, an approximately inertial frame with spatial coordinates fixed on the centre of the Sun, known as the Sun-centred frame (SCF), is introduced as a convenient frame to report constraints on the SME coefficients [26–28]. In the SCF, the coefficients are typically assumed to be spacetime constants, implying the preservation of translation invariance and the conservation of four-momentum [14]. Thus, in another frame rotating with respect to the SCF, such as the laboratory frame, the coefficients will oscillate as a function of time. To make this time dependence explicit, the coefficients appearing in the laboratory-frame cross sections are re-expressed in terms of the SCF coefficients by performing the appropriate Lorentz transformation $\Lambda^\mu{}_\nu$. For example, the transformation for the c -type coefficients is

$$c_{\text{lab}}^{\mu\nu} = \Lambda^\mu{}_\alpha \Lambda^\nu{}_\beta c_{\text{SCF}}^{\alpha\beta}. \quad (12)$$

In what follows, coefficients that appear with Greek and numeric indices denote laboratory-frame coefficients and those with capital Latin indices denote SCF coefficients. After performing this transformation and re-expressing the laboratory-frame coefficients, the laboratory cross sections are functions of the fixed SCF coefficients and sinusoidal functions with periods controlled by the length of the sidereal day. The boost of the Earth with respect to the Sun, $\beta_\oplus \approx 10^{-4}$, is suppressed relative to the effect of Earth's rotation by several orders of magnitude and can be neglected. Also, the fact that the Earth's orbit is translated with respect to the SCF has no physical effect because of translation invariance. Therefore, the transformation $\Lambda^\mu{}_\nu$ in Eq. (12) is well approximated as a pure rotation: $\Lambda^0{}_0 = 1$, $\Lambda^\mu{}_0 = 0 = \Lambda^0{}_\mu$ and $\Lambda^i{}_j = R^i{}_j$ ($i, j = 1, 2, 3$) is an orthogonal matrix.

The SCF is depicted in Fig. 2. It is defined by coordinates $X^\mu = (T, X, Y, Z)$ as follows: $T = 0$ is identified with the date of the 2000 vernal equinox, March 20, 2000 at 7:35 UTC; the Z axis is aligned with the Earth's rotation axis; the X axis points from the Earth to the Sun at $T = 0$; and the Y axis completes the right-handed coordinate system. At $T = 0$, the Earth's equator lies in the XY plane and the longitude $\lambda_0 \approx 66.25^\circ$ will observe the Sun directly overhead, towards the local zenith. Therefore, $T = 0$ is a suitable moment for easily relating the SCF coordinates to the laboratory-frame coordinates. The small effects

of the Earth's non-circular orbit can be neglected. For the ZEUS detector, the co-latitude, orientation of the electron/positron- or proton-beam direction and the local sidereal time T_{\oplus} must be specified. The zero of T_{\oplus} is defined as one of the moments when the y axis of the laboratory is parallel to the SCF Y axis, which on the date of the equinox occurs shortly after $T = 0$. In other words, since HERA is not situated at the longitude λ_0 , but the longitude $\lambda \approx 9.88^\circ$, $T_{\oplus} \neq T$. Instead, T_{\oplus} is related to T by an offset given by [20]

$$T - T_{\oplus} = \frac{\lambda_0 - \lambda}{360^\circ} T_{\text{sidereal}} = 3.748 \text{ h} , \quad (13)$$

where $T_{\text{sidereal}} = 23 \text{ h } 56 \text{ min } 4.091 \text{ s}$ is the sidereal day. The first occurrence for which $T_{\oplus} = 0$ is therefore approximately 3.75 hours after the 2000 vernal equinox, or March 20, 2000 at 11:20 UTC. This is the chosen initial condition for referencing the time of ZEUS $e^\pm p$ events. The co-latitude of HERA is $\chi \approx 36.4^\circ$, and the electron/positron-beam orientation for ZEUS is $\Psi \approx 20^\circ$ south of west. Finally, the net rotation R from the proton-beam direction in the laboratory frame to the SCF is given by

$$R = \begin{pmatrix} 1 & 0 & 0 \\ 0 & 0 & 1 \\ 0 & -1 & 0 \end{pmatrix} \begin{pmatrix} \cos \Psi & \sin \Psi & 0 \\ -\sin \Psi & \cos \Psi & 0 \\ 0 & 0 & 1 \end{pmatrix} \begin{pmatrix} \cos \chi \cos \omega_{\oplus} T_{\oplus} & \cos \chi \sin \omega_{\oplus} T_{\oplus} & -\sin \chi \\ -\sin \omega_{\oplus} T_{\oplus} & \cos \omega_{\oplus} T_{\oplus} & 0 \\ \sin \chi \cos \omega_{\oplus} T_{\oplus} & \sin \chi \sin \omega_{\oplus} T_{\oplus} & \cos \chi \end{pmatrix} , \quad (14)$$

where $\omega_{\oplus} = 2\pi/T_{\text{sidereal}}$ is the Earth's sidereal frequency. Performing the rotation R to express the laboratory-frame coefficients in terms of the constant SCF coefficients induces a sidereal-time dependence at multiples of the Earth's sidereal frequency.

As an example, the transformation of the coefficient c_u^{33} reads:

$$\begin{aligned} c_u^{33} &= \frac{1}{2}(c_u^{XX} + c_u^{YY}) (\cos^2 \chi \sin^2 \Psi + \cos^2 \Psi) + c_u^{ZZ} \sin^2 \chi \sin^2 \Psi \\ &\quad - 2c_u^{XZ} \sin \chi \sin \Psi [\cos \chi \sin \Psi \cos(\omega_{\oplus} T_{\oplus}) + \cos \Psi \sin(\omega_{\oplus} T_{\oplus})] \\ &\quad - 2c_u^{YZ} \sin \chi \sin \Psi [\cos \chi \sin \psi \sin(\omega_{\oplus} T_{\oplus}) - \cos \psi \cos(\omega_{\oplus} T_{\oplus})] \\ &\quad + c_u^{XY} [(\cos^2 \chi \sin^2 \Psi - \cos^2 \Psi) \sin(2\omega_{\oplus} T_{\oplus}) - \cos \chi \sin(2\Psi) \cos(2\omega_{\oplus} T_{\oplus})] \\ &\quad + \frac{1}{2}(c_u^{XX} - c_u^{YY}) [(\cos^2 \chi \sin^2 \Psi - \cos^2 \Psi) \cos(2\omega_{\oplus} T_{\oplus}) + \cos \chi \sin(2\Psi) \sin(2\omega_{\oplus} T_{\oplus})] , \end{aligned} \quad (15)$$

where it is seen that the terms proportional to $(c_u^{XX} + c_u^{YY})$ and c_u^{ZZ} possess no sidereal-time dependence, the terms proportional to c_u^{XZ} and c_u^{YZ} oscillate with angular frequency ω_{\oplus} and the terms proportional to c_u^{XY} and $(c_u^{XX} - c_u^{YY})$ oscillate with angular frequency $2\omega_{\oplus}$.

After expressing the cross section given in Eq. (5) in terms of the SCF coefficients, only the following 18 combinations of coefficients yield sidereal-time oscillations:

$$c_f^{TX} , c_f^{XZ} , c_f^{TY} , c_f^{YZ} , c_f^{XY} \text{ and } (c_f^{XX} - c_f^{YY}) , \quad (16)$$

with $f = u, d$, and s . Analogously, after the replacement $a_{\text{lab}}^{(5)\mu\alpha\beta} = \Lambda^\mu_\nu \Lambda^\alpha_\rho \Lambda^\beta_\sigma a_{\text{SCF}}^{(5)\nu\rho\sigma}$ in Eq. (8), it is found that, for each quark, only the following 12 combinations of coefficients yield sidereal-time oscillations:

$$\begin{aligned} & (a_{\text{S}f}^{(5)TXX} - a_{\text{S}f}^{(5)TTY}), (a_{\text{S}f}^{(5)XXZ} - a_{\text{S}f}^{(5)YYZ}), a_{\text{S}f}^{(5)TXY}, a_{\text{S}f}^{(5)TXZ}, a_{\text{S}f}^{(5)TYZ}, a_{\text{S}f}^{(5)XXX}, \\ & a_{\text{S}f}^{(5)XXY}, a_{\text{S}f}^{(5)XYY}, a_{\text{S}f}^{(5)XYZ}, a_{\text{S}f}^{(5)XZZ}, a_{\text{S}f}^{(5)YYY} \text{ and } a_{\text{S}f}^{(5)YZZ}, \end{aligned} \quad (17)$$

giving a total of 36 combinations. For antiquarks with flavour $f = \bar{u}, \bar{d}$ and \bar{s} , the coefficients effectively appear in the cross section Eq. (8) with opposite signs relative to the quark coefficients. Since the contributions from s and \bar{s} are equal, only the 24 coefficients for $f = u$ and d are considered. The c - and $a^{(5)}$ -type coefficients in Eqs. (16) and (17) induce oscillations with frequencies up to $2\omega_\oplus$ and $3\omega_\oplus$, respectively. More generally, an SCF coefficient with n Lorentz indices will include sidereal oscillations up to $n\omega_\oplus$.

The expected sensitivities to the c - and $a^{(5)}$ -type coefficients that can be extracted from DIS data have been studied [6, 7, 9]. In particular, the combined DIS cross sections from ZEUS and H1 [21] have been used to estimate the sensitivity of a sidereal-time study using these data. For each value in the (x_{BJ}, Q^2) plane, potential constraints based on four sidereal intervals have been extracted. A subset of simulated results describing the sensitivity to the c - and $a^{(5)}$ -type coefficients as a function of phase are shown in Fig. 3. It is observed that the sensitivities to the c - and $a^{(5)}$ -type coefficients are roughly at levels of 10^{-4} and 10^{-6} GeV $^{-1}$, respectively.

3 Experimental set-up and data selection

The analysis is based on events collected with the ZEUS detector at HERA during the HERA II run period 2003–2007. For this configuration, the initial-state proton- and electron/positron-beam energies were $E_p = 920$ GeV and $E_e = 27.5$ GeV, respectively, with a centre-of-mass energy of $\sqrt{s} = 318$ GeV and an integrated luminosity 372 pb $^{-1}$. Details of the ZEUS detector are given elsewhere [29].

The NC DIS events were selected with the following criteria [30]:

- the final-state lepton was identified using an algorithm based on a neural network [31, 32], giving a probability larger than 90%;
- the energy of the final-state lepton $E'_e > 10$ GeV to ensure a high electron-identification efficiency;
- $Q^2 > 5$ GeV 2 ;
- $\theta_e > 1$ rad, where θ_e is the scattering angle between the outgoing lepton and incoming proton direction to ensure the high efficiency of the electron-identification algorithm. This provides an upper limit on Q^2 ;

- the scattered lepton was required to enter the calorimeter at a radial position larger than 15 cm, implying an upper bound on the lepton scattering angle $\theta_e \lesssim 3$ rad;
- the position of the event vertex along the laboratory z axis was required to be within 30 cm of its nominal value and the transverse distance of the event vertex from the interaction point was required to be within 0.5 cm, to reject background;
- $47 \text{ GeV} < E - p_z < 69 \text{ GeV}$, where E and p_z are the total energy and z -component of the final state, to reject background.

This selection resulted in $4.5 \cdot 10^7$ events covering the kinematic range $7.7 \cdot 10^{-5} < x_{\text{Bj}} < 1$ and $5 < Q^2 < 8800 \text{ GeV}^2$.

4 Analysis method

Possible variations of cross sections with periodicity T_p were studied. The starting point was the triple differential DIS cross section

$$\frac{d\sigma}{dx_{\text{Bj}} dQ^2 d\phi_{T_p}}, \quad (18)$$

where the temporal phase $\phi_{T_p} = \text{Mod}(T_{\oplus}, T_p)/T_p$ is the phase of a given DIS event with the time stamp T_{\oplus} for the chosen period, T_p , and is defined in the range $[0, 1]$. Within the SME, only $T_p = T_{\text{sidereal}}$ yields a non-vanishing dependence on ϕ_{T_p} , as the sidereal angle is $\omega_{\oplus} T_{\oplus}$. If a different period is used, the time dependence quickly averages out; the larger the difference between T_p and T_{sidereal} , the faster this occurs.

It was necessary to eliminate uncertainties related to the instantaneous luminosity, which decays over several hours during each fill. To do so would have required the integrated luminosity to be measured roughly every minute, but this information was not available. Instead, double ratios of the form

$$r(\text{PS}_1, \text{PS}_2) = \frac{\int_{\text{PS}_1} dx_{\text{Bj}} dQ^2 \frac{d\sigma}{dx_{\text{Bj}} dQ^2 d\phi_{T_p}} / \int_{\text{PS}_1} dx_{\text{Bj}} dQ^2 d\phi_{T_p} \frac{d\sigma}{dx_{\text{Bj}} dQ^2 d\phi_{T_p}}}{\int_{\text{PS}_2} dx_{\text{Bj}} dQ^2 \frac{d\sigma}{dx_{\text{Bj}} dQ^2 d\phi_{T_p}} / \int_{\text{PS}_2} dx_{\text{Bj}} dQ^2 d\phi_{T_p} \frac{d\sigma}{dx_{\text{Bj}} dQ^2 d\phi_{T_p}}}, \quad (19)$$

where PS_1 and PS_2 are two regions of the (x_{Bj}, Q^2) kinematic range, for which luminosity uncertainty cancels, were used. Essential properties of Eq. (19) are that it is independent of the luminosity and equal to unity in the absence of SME effects. Evaluating the contributions involving integrations of ϕ_{T_p} results in zero sensitivity to SME coefficients and when summing the contributions of all quark flavours produces the Standard Model cross section. Moreover, if the regions $\text{PS}_{1,2}$ are chosen appropriately, the double ratio shows a strong ϕ_{T_p} dependence in the presence of SME effects. As explained in Section (2.2), a strong sensitivity at low x_{Bj} ($\approx 10^{-5}$ – 10^{-3}) for the c -type coefficients and $x_{\text{Bj}} \gtrsim 10^{-3}$

for the $a^{(5)}$ -type coefficients is expected. However, for $x_{Bj} \lesssim 10^{-4}$ and $x_{Bj} \gtrsim 10^{-2}$, fewer DIS events are available and thus the statistical uncertainties become larger. The x_{Bj} distribution is sharply peaked around $x_{Bj} \approx 10^{-3}$, implying a statistically optimal choice of cut x_c in the (x_{Bj}, Q^2) kinematic range.

In evaluating Eq. (19) for several values of x_c , it was found that the combinations simultaneously giving the most sensitivity to the cross section while producing the lowest statistical uncertainties are $x_c = 5 \cdot 10^{-4}$ and 10^{-3} for c - and $a^{(5)}$ -type coefficients, respectively. However, as no higher-order QCD corrections are included in the cross sections given in Eqs. (5) and (8), potential large corrections are expected, of the order $[\alpha_s(Q^2) \log 1/x_{Bj}]^n$ at very low x_{Bj} , which need to be resummed. Numerically, such effects could shift the value of x entering the PDFs. Thus, x would not coincide with x_{Bj} . This issue is partially alleviated by cutting at moderate values $x_{Bj} \gtrsim 10^{-3}$, where QCD corrections have a smaller influence. The value $x_c = 10^{-3}$ was therefore chosen for both the c - and $a^{(5)}$ -type coefficients.

By employing Eqs. (5) and (8), the integrations above and below $x_c = 10^{-3}$ were performed for the kinematic range in x_{Bj}, Q^2 and θ_e as described in Section 3. The double ratios from Eq. (19) evaluated in the laboratory frame are:

$$\begin{aligned}
r_c(x_{Bj} > x_c, x_{Bj} < x_c) &= 1 - 12.8 c_u^{03} - 13.9 c_u^{33} + 0.9 (c_u^{11} + c_u^{22}) \\
&\quad - 4.2 c_d^{03} - 2.9 c_d^{33} + 0.1 (c_d^{11} + c_d^{22}) \\
&\quad - 3.4 c_s^{03} - 1.8 c_s^{33} + 2.9 \cdot 10^{-2} (c_s^{11} + c_s^{22}), \quad (20)
\end{aligned}$$

$$\begin{aligned}
r_{a^{(5)}}(x_{Bj} > x_c, x_{Bj} < x_c) &= 1 - 6.1 \cdot 10^3 a_u^{(5)003} + 6.8 \cdot 10^3 a_u^{(5)033} - 2.5 \cdot 10^3 a_u^{(5)333} \\
&\quad + 5.0 \cdot 10^2 (a_u^{(5)113} + a_u^{(5)223} - a_u^{(5)011} - a_u^{(5)022}) \\
&\quad - 4.1 \cdot 10^2 a_d^{(5)003} + 4.7 \cdot 10^2 a_d^{(5)033} - 1.7 \cdot 10^2 a_d^{(5)333} \\
&\quad + 40 (a_d^{(5)113} + a_d^{(5)223} - a_d^{(5)011} - a_d^{(5)022}), \quad (21)
\end{aligned}$$

where the numerical prefactors multiplying the $a^{(5)}$ -type coefficients in the latter expression are in units of GeV. These expressions only contain terms linear in the coefficients, as higher-order corrections are greatly suppressed. The ratio $r_{a^{(5)}}$ has negligible sensitivity to $a_s^{(5)\mu\alpha\beta}$ because of the nearly identical and opposite-in-sign s, \bar{s} contributions to the cross section, see Eq. (8). After re-expressing the laboratory-frame coefficients appearing in Eqs. (20) and (21) in terms of rotational-symmetry violating combinations of the SCF coefficients described in Section 2.3 using Eq. (14), it is found that 42 SCF coefficients result in deviations of r_c or $r_{a^{(5)}}$ from unity. Comparisons between these double ratios and the analogous ratios constructed purely from the binned DIS events were made under the assumption of constant efficiency corrections. Constraints were placed on each coefficient one at a time by setting all others to zero, in accordance with standard practice [2].

5 Systematic effects

5.1 Initial considerations

A luminosity-independent ratio, Eq. (19), that does not possess a sizeable dependence on SME effects was used to test the data. The ratio $r(Q^2 > Q_c^2, Q^2 < Q_c^2)$ with $Q_c^2 = 20 \text{ GeV}^2$ fulfills this requirement.

The data rate in the detector is not constant. In particular, more data were taken in the evenings than in the morning. To display this effect, the entire DIS selection in the two Q^2 regions was binned using the solar phase $\phi_{\text{solar}} = \text{Mod}(T_{\oplus}, T_{\text{solar}})/T_{\text{solar}}$ with $T_{\text{solar}} = 24 \text{ h}$. In Fig. 4(a), the resulting normalised count of the events passing the selection described in Section 3 is displayed. It is clear that an $\mathcal{O}(25\%)$ effect is present. Switching from solar to sidereal binning with $\phi_{\text{sidereal}} = \text{Mod}(T_{\oplus}, T_{\text{sidereal}})/T_{\text{sidereal}}$ dilutes this solar-phase dependence for long data-taking periods. As shown in Fig. 4(b), sidereal dilution over ≈ 5 years reduces the effect to $\mathcal{O}(10\%)$, but is not sufficient to erase it completely. The dilution effect of a much longer period of data taking can be simulated by binning using a short period. In Fig. 4(c), a plot of the same data binned using a $T_p = 1 \text{ h}$ period with $\phi_{\text{test}} = \text{Mod}(T_{\oplus}, 1 \text{ h})/1 \text{ h}$ is shown. The initial solar-phase dependence disappears almost completely. Figure 4(d) shows that for a period slightly longer than the solar day, $T_p = 24 \text{ h } 4 \text{ min}$, a similar level of dilution as for the sidereal-phase binning in Fig. 4(b) is observed. For each choice of phase, the histograms for events with Q^2 above and below Q_c^2 closely track each other and their ratios are consistent with unity.

An important question is whether systematic uncertainties can be neglected. A partial answer can be found by performing Kolmogorov–Smirnov (KS) tests on the binned ratios $r(Q_c)$. This test calculates the probability that the observed distributions are compatible with an unsorted sampling of a normal distribution with mean unity and standard deviation identical to the observed statistical uncertainties. The ratios are plotted in different numbers of bins N_{bins} to estimate the size of systematic relative to statistical effects. The results are presented for $T_p = 24 \text{ h}$ in Fig. 5 and for $T_p = T_{\text{sidereal}}$ in Fig. 6. It is observed that, independently of the period, $T_p = 24 \text{ h}$ or $T_p = T_{\text{sidereal}}$, and of the number of bins, the results are statistically compatible with unity as indicated by the high KS probabilities. The impact of systematic uncertainties appears to be minimal in these distributions. However, this is insufficient to conclude that systematic uncertainties can be neglected when looking at sidereal and solar distributions for SME-sensitive x_c ratios given by Eqs. (20) and (21). This is because low- and high- x_{Bj} regions, where the trigger behaves differently and could be affected by the instantaneous luminosity, could be subject to systematic effects which would not cancel in the ratio defined in Eq. (19).

As long as each bin is considerably smaller than the duration of a fill, which is typically several hours, (e.g., for $T_p = 1 \text{ h}$, each bin is between 0.6 min ($N_{\text{bins}} = 100$) and 2.4 min ($N_{\text{bins}} = 25$)), it is expected that all such effects will average out. On the other hand, for

the solar or sidereal phase, the time bins range between ≈ 15 min and 1 h. It is possible that fluctuations in trigger efficiencies and accelerator effects could affect high-luminosity and low-luminosity parts of the fill differently. This might result in non-negligible residual effects in the solar- and sidereal-ratio distributions.

5.2 Data analysis of x_c and Monte Carlo simulation

When separating the kinematic range into regions above and below the cut $x_c = 10^{-3}$, the normalised counts presented in Fig. 7 strongly resemble those from Q_c^2 cuts in Fig. 4. Similarly, in light of the discussion in Section 5.1, it is expected that the $T_p = 1$ h distributions for the ratios $r(x_{Bj} > x_c, x_{Bj} < x_c)$ given explicitly in Eqs. (20) and (21) will be distributed around unity and will be dominated by statistical uncertainties. As discussed, any potential solar and sidereal effects should be removed when binning data using a test period much smaller than 24 h. This is indeed the case, as can be seen from the results for ϕ_{test} presented in Fig. 8. In contrast to the Q_c^2 distributions for all phases, the solar phases for the x_c distributions contain more structure, as is immediately evident from Fig. 9.

The $N_{\text{bins}} = 25$ configuration exhibits a 1% KS probability, implying the presence of systematics that are unaccounted for. This is also apparent as the one-sigma spreads, particularly for the smaller $N_{\text{bins}} = 25$ case, are much wider than the uncertainty bars on the central values, with larger deviation around unity than in the test-phase case (see Fig. 8). This is not sufficient to identify the origin of the additional systematic effects. However, an estimate of this systematic contribution for a given N_{bins} may be obtained by calculating

$$\sigma_{\text{syst}} \approx \sqrt{\sigma^2 - \sigma_{\text{stat}}^2}, \quad (22)$$

where σ and σ_{stat} are the standard deviation and mean statistical uncertainty of the points of the distribution, respectively.

As already stressed, the observed systematic effects are not directly connected to large fluctuations of the instantaneous luminosity. They have not been previously observed because such small uncertainties were negligible in all previous ZEUS analyses. This was confirmed by means of a Monte Carlo study. Inclusive DIS events with $Q^2 > 4 \text{ GeV}^2$ were generated with DJANGO 1.6 [33] interfaced to ARIADNE [34–37]. The CTEQ5D [38] PDFs were used. The events were subsequently passed through the ZEUS detector and trigger simulations based on GEANT 3 [39]. The Monte Carlo events contain leading-order QCD corrections plus parton showering at matrix-element level. Also, the x in the PDFs is no longer identified with x_{Bj} , although this is not expected to affect results significantly.

The parton-level calculation is based purely on the Standard Model and does not introduce any direct time dependence. The generated events do not possess time stamps. However, the detector response and the trigger configuration depend on the instantaneous luminosity and may change over time. Data events are grouped into blocks with the same detector and

trigger configurations and, for each of these blocks, appropriate Monte Carlo events were generated. In order to include time dependence in the Monte Carlo events and to simulate accurately the impact of the variable instantaneous luminosity over the course of 5 years, the following procedure was performed. For each luminosity block containing a given number of data events, all time stamps were extracted and assigned Monte Carlo events randomly selected from all those events generated with the same detector and trigger status. The obtained Monte Carlo sample simulates accurately any time dependence associated with the instantaneous luminosity and the detector response.

This study was performed on a subset of experimental data (namely electron data taken in 2006) corresponding to an integrated luminosity of 54.8 pb^{-1} . It was found that phase distributions obtained from Monte Carlo events are perfectly compatible with statistical uncertainties alone: no evidence of any residual systematic contribution to the fluctuation of the binned central values around unity is observed in these simulations. This is also confirmed by comparing the one-sigma spreads of data and Monte Carlo, with the former being much larger than the latter (and the latter being in agreement with the statistical uncertainties alone).

This analysis shows that the residual systematic uncertainties observed in data are not modelled in existing Monte Carlo simulations. As explained above, a reasonable strategy is to use the difference in quadrature between the one-sigma spreads and the corresponding statistical uncertainties as an estimate of the additional systematics. Note that, in the present study, all previously known sources of systematic uncertainties cancel.

As additional checks, separate studies involving events taken under different trigger settings, which are constant within each luminosity block, have been performed. No discernible impact on the presence of the systematic uncertainties discussed above is observed.

5.3 Estimated systematic uncertainties

The binned solar x_c analyses clearly indicate the presence of an unknown, substantial, and pervasive time-dependent systematic effect with mean systematic uncertainty $\bar{\sigma}_{\text{syst}} \approx 0.26\%$. The extraction of systematic uncertainties for periods $T_{\text{sidereal}} \approx T_{\text{solar}} - 4 \text{ min}$ ($\bar{\sigma}_{\text{syst}} \approx 0.18\%$) and $2T_{\text{solar}} - T_{\text{sidereal}} \approx T_{\text{solar}} + 4 \text{ min}$ ($\bar{\sigma}_{\text{syst}} \approx 0.11\%$) both result in smaller systematic uncertainties relative to the period T_{solar} , further suggesting a possible unaccounted for solar-periodic effect, which may be a consequence of the operation of the experiment. The systematic uncertainties on the ratio binned in sidereal time may therefore reflect a dilution of the observed potential solar-periodic effect. While, at this stage, a claim of a genuine solar-time effect cannot be made, there is no significant indication of a comparable sidereal-time effect. This establishes a baseline for extracting constraints. Under the assumption of a genuine solar systematic effect, the $2T_{\text{solar}} - T_{\text{sidereal}}$ distributions determine the dilution of the solar systematic when changing the period by +4 minutes; in fact, dilution effects for very small positive or negative time shifts are very similar. This

method makes possible an estimate of the systematic uncertainties on the sidereal-time distributions without risking an absorption of potential genuine sidereal signals.

In the next section, the constraints on the SME coefficients are extracted using $N_{\text{bins}} = 100$. For consistency, the systematic uncertainty used in the constraint-setting procedure is also extracted from the $2T_{\text{solar}} - T_{\text{sidereal}}$ distribution with 100 bins. This distribution is presented in Fig. 10 and yields $\sigma_{\text{syst}} \approx 0.16\%$. A fuller understanding of this systematic effect is left for future studies and is beyond the scope of the present analysis.

6 Constraints on effective couplings

The sidereal-phase distributions of the ratio of normalised counts for x_{B_j} above and below $x_c = 10^{-3}$ are shown in Fig. 11. This is the main result of this paper from which constraints on the SME coefficients will be extracted. Compared to the solar-phase case, much higher KS probabilities are observed. To extract constraints, the following procedure was performed. The laboratory coefficients in the ratios Eqs. (20) and (21) were replaced with the SCF coefficients as explained in Section 2.3, replacing one coefficient at a time. The ratios then depend on the local sidereal angle $\theta_{\oplus} = \omega_{\oplus} T_{\oplus}$. For a given bin i , the theoretical ratios r_i^{theo} were calculated as

$$r_i^{\text{theo}} = \frac{N_{\text{bins}}}{2\pi} \int_{\frac{2\pi(i-1)}{N_{\text{bins}}}}^{\frac{2\pi i}{N_{\text{bins}}}} r(x > x_c, x < x_c; \theta_{\oplus}) d\theta_{\oplus}, \quad (23)$$

where $i = 1, \dots, N_{\text{bins}}$. This quantity can be compared directly with the experimental sidereal ratios r_i^{exp} . A χ^2 function was constructed

$$\chi^2 = \frac{1}{\sigma_{\text{tot}}^2} \sum_{i=1}^{N_{\text{bins}}} (r_i^{\text{exp}} - r_i^{\text{theo}})^2, \quad (24)$$

for each of the 42 observable SCF coefficients. The total uncertainty σ_{tot} in Eq. (24) is given by combining in quadrature the statistical uncertainty ($[\sigma_{\text{stat}}]_{N_{\text{bins}}=100} = 0.32\%$) and the systematic uncertainty estimated in the previous section ($\sigma_{\text{syst}} = 0.16\%$) taken as an additional random uncertainty at each point, so that $\sigma_{\text{tot}} = 0.35\%$.

The χ^2 in the Standard Model is obtained by setting all the SME coefficients to zero (the theory prediction in the Standard Model is identically 1 in each phase bin), and is 113.8 for 100 degrees of freedom. The p -value for this goodness-of-fit (GOF) test is $p_{\text{SM}} = 0.16$, indicating a reasonable description of the data by the Standard Model. In Tables 1 and 2, lower (upper) values of each coefficient are presented, below (above) which the p -values for the same χ^2 GOF test are smaller than 0.05. These values are indicative of the disfavoured ranges for which the c -type coefficients are roughly at the level of 10^{-4} for the u -quark

coefficients and 10^{-3} for the d - and s -quark coefficients. The corresponding ranges for the $a^{(5)}$ -type coefficients are mostly at the level of 10^{-7} GeV^{-1} for the u -quark coefficients and 10^{-6} GeV^{-1} for the d -quark coefficients.

Figure 12 shows the time dependence associated with non-vanishing c_u^{TY} , $c_u^{XX} - c_u^{YY}$ and $a_{Su}^{(5)XXY}$ coefficients. These three coefficients have been chosen because they are examples of time dependence with angular frequencies ω_{\oplus} , $2\omega_{\oplus}$ and $3\omega_{\oplus}$, respectively. In each case, the data points are identical to those presented in Fig. 11, the solid and dashed curves correspond to selected values of the disfavoured regions presented in Tables 1 and 2, and the dotted curves correspond to coefficients that are roughly an order of magnitude larger.

Comparison with existing constraints is informative [2]. For the c -type coefficients, the results derived in this work represent the first constraints using sidereal oscillations. For the u and d quarks, there are existing and considerably more stringent constraints derived from interpretations of cosmic-ray measurements [40]. The latter constraints rest on a number of model-dependent assumptions, so that direct comparison between those results and what is presented here requires caution. The constraints on the s -quark coefficients are derived for the first time. The results for the $a^{(5)}$ -type coefficients are the first of their kind. One potential point of comparison would be the constraints on effective $a^{(5)}$ -type coefficients for protons, as reported in Table D11 [2]. Using hydrogen 1S–2S transitions, similar combinations of proton constraints are currently at the level of 10^{-7} – 10^{-8} GeV^{-1} , which is similar in magnitude to that found for u -quark $a^{(5)}$ -type coefficients [41].

7 Summary and outlook

An analysis searching for effective coefficients parameterising Lorentz and CPT violation in the light-quark sector has been performed using ZEUS $e^{\pm}p$ DIS NC data at HERA. Conservative estimates of previously unknown time-dependent systematic uncertainties independent of instantaneous luminosity and trigger configuration have been made by binning and analysing events as a function of the sidereal-rotation frequency of the Earth. By combining binned sidereal statistical uncertainties with systematic uncertainties in quadrature, the data are shown to be compatible with the Standard Model. First constraints have been placed on the 24 combinations of the non-renormalisable, CPT-violating, and spin-independent $a^{(5)}$ -type operators associated with rotationally anisotropic u - and d -quark effects. For the renormalisable CPT-preserving c -type coefficients, the first constraints have been placed on the six rotationally anisotropic s -quark coefficients and the first experimental constraints have been extracted on the analogous 12 u - and d -quark coefficients. In total, 42 coefficients have been constrained, 30 for the first time.

Partonic-physics studies of fundamental symmetries and experimental analyses searching for unconventional time-dependent signatures are in their infancy. A statistically significant

ant indication of Lorentz or related fundamental-symmetry violation in EFT would not unequivocally indicate the presence of phenomena outside the description of quantum field theory and metric theories of gravity. Nonetheless, such a discovery would indicate the presence of new physics, which is a strong motivation for further work in this area.

Acknowledgements

We appreciate the contributions to the construction, maintenance and operation of the ZEUS detector of many people who are not listed as authors. The HERA machine group and the DESY computing staff are especially acknowledged for their success in providing excellent operation of the collider and the data-analysis environment. We thank the DESY directorate for their strong support and encouragement.

References

- [1] A.A. Michelson and E.W. Morley, On the Relative Motion of the Earth and the Luminiferous Ether. *Am. J. Sci.* **34**, 333 (1887)
- [2] V.A. Kostelecký and N. Russell, Data Tables for Lorentz and CPT Violation. *Rev. Mod. Phys.* **83**, 11 (2011). [arXiv:0801.0287v15](#)
- [3] S.I. Karpikov, D. Tlisov, and D. Kirpichnikov, Space anisotropy search at colliders. *Phys. Atom. Nucl.* **81**, 257 (2018). [arXiv:1612.02217](#)
- [4] M.S. Berger, V.A. Kostelecký, and Z. Liu, Lorentz and CPT Violation in Top-Quark Production and Decay. *Phys. Rev. D* **93**, 036005 (2016). [arXiv:1509.08929](#)
- [5] D0 Collaboration, V.M. Abazov et al., Search for violation of Lorentz invariance in top quark pair production and decay. *Phys. Rev. Lett.* **108**, 261603 (2012). [arXiv:1203.6106](#)
- [6] V.A. Kostelecký, E. Lunghi, and A.R. Vieira, Lorentz Violation and Deep Inelastic Scattering. *Phys. Lett. B* **769**, 272 (2017). [arXiv:1610.08755](#)
- [7] E. Lunghi and N. Sherrill, Lorentz violation and the electron-ion collider. *Phys. Rev. D* **98**, 115018 (2018). [arXiv:1805.11684](#)
- [8] V.A. Kostelecký and Z. Li, Gauge Field Theories with Lorentz-Violating Operators of Arbitrary Dimension. *Phys. Rev. D* **99**, 056016 (2019). [arXiv:1812.11672](#)
- [9] V.A. Kostelecký et al., Lorentz and CPT Violation in Partons. *JHEP* **04**, 143 (2020). [arXiv:1911.04002](#)
- [10] E. Lunghi et al., Quark-sector Lorentz violation in Z -boson production. *JHEP* **04**, 228 (2021). [arXiv:2011.02632](#)
- [11] S. Weinberg, Effective Field Theory, Past and Future. *PoS CD09*, 001 (2009). [arXiv:0908.1964](#)
- [12] D. Colladay and V.A. Kostelecký, CPT Violation and the Standard Model. *Phys. Rev. D* **55**, 6760 (1997). [arXiv:hep-ph/9703464](#)
- [13] D. Colladay and V.A. Kostelecký, Lorentz-Violating Extension of the Standard Model. *Phys. Rev. D* **58**, 116002 (1998). [arXiv:hep-ph/9809521](#)
- [14] V.A. Kostelecký, Gravity, Lorentz Violation, and the Standard Model. *Phys. Rev. D* **69**, 105009 (2004). [arXiv:hep-th/0312310](#)
- [15] V.A. Kostelecký and Z. Li, Backgrounds in gravitational effective field theory. *Phys. Rev. D* **103**, 024059 (2021). [arXiv:2008.12206](#)
- [16] O.W. Greenberg, CPT violation implies violation of Lorentz invariance. *Phys. Rev. Lett.* **89**, 231602 (2002). [arXiv:hep-ph/0201258](#)

- [17] R. Bluhm, Overview of the SME: Implications and phenomenology of Lorentz violation. *Lect. Notes Phys.* **702**, 191 (2006). [arXiv:hep-ph/0506054](#)
- [18] J.D. Tasson, What Do We Know About Lorentz Invariance? *Rept. Prog. Phys.* **77**, 062901 (2014). [arXiv:1403.7785](#)
- [19] B.R. Edwards and V.A. Kostelecký, Searching for CPT Violation with Neutral-Meson Oscillations. *Phys. Lett. B* **795**, 620 (2019). [arXiv:1907.05206](#)
- [20] Y. Ding and V.A. Kostelecký, Lorentz-violating spinor electrodynamics and Penning traps. *Phys. Rev. D* **94**, 056008 (2016). [arXiv:1608.07868](#)
- [21] H1 and ZEUS Collaborations, H. Abramowicz et al., Combination of measurements of inclusive deep inelastic $e^\pm p$ scattering cross sections and QCD analysis of HERA data. *Eur. Phys. J. C* **75**, 580 (2015). [arXiv:1506.06042](#)
- [22] CMS Collaboration, A.M. Sirunyan et al., Measurement of the differential Drell-Yan cross section in proton-proton collisions at $\sqrt{s} = 13$ TeV. *JHEP* **12**, 059 (2019). [arXiv:1812.10529](#)
- [23] A.D. Martin et al., Parton distributions for the LHC. *Eur. Phys. J. C* **63**, 189 (2009). [arXiv:0901.0002](#)
- [24] E. Godat, ManeParse: Mathematica Toolbox for PDF Uncertainties and Application to New Physics Searches. Proceedings, Meeting of the APS Division of Particles and Fields (DPF 2015): Ann Arbor, Michigan, USA, 4-8 Aug 2015. [arXiv:1510.06009](#)
- [25] D.B. Clark, E. Godat and F.I. Olness, ManeParse: A Mathematica reader for Parton Distribution Functions. *Comput. Phys. Commun.* **216**, 126 (2017). [arXiv:1605.08012](#)
- [26] V.A. Kostelecký and M. Mewes, Signals for Lorentz Violation in Electrodynamics. *Phys. Rev. D* **66**, 056005 (2002). [arXiv:hep-ph/0205211](#)
- [27] R. Bluhm et al., Clock comparison tests of Lorentz and CPT symmetry in space. *Phys. Rev. Lett.* **88**, 090801 (2002). [arXiv:hep-ph/0111141](#)
- [28] R. Bluhm et al., Probing Lorentz and CPT violation with space based experiments. *Phys. Rev. D* **68**, 125008 (2003). [arXiv:hep-ph/0306190](#)
- [29] U. Holm et al., The ZEUS detector. ZEUS-STATUS-REPT-1993
- [30] ZEUS Collaboration, I. Abt et al., Two-particle azimuthal correlations as a probe of collective behaviour in deep inelastic ep scattering at HERA. *JHEP* **04**, 070 (2020). [arXiv:1912.07431](#)
- [31] H. Abramowicz, A. Caldwell and R. Sinkus, Neural network based electron identification in the ZEUS calorimeter. *Nucl. Instrum. Meth. A* **365**, 508 (1995). [arXiv:hep-ex/9505004](#)

- [32] R. Sinkus and T. Voss, Particle identification with neural networks using a rotational invariant moment representation. *Nucl. Instrum. Meth. A* **391**, 360 (1997)
- [33] G.A. Schuler and H. Spiesberger, DJANGO: The Interface for the event generators HERACLES and LEPTO. *Proc. Workshop on Physics at HERA*, W. Buchmüller and G. Ingelman (eds.), Vol. 3, p. 1419. Hamburg, Germany, DESY (1991)
- [34] U. Pettersson, ARIADNE: A Monte Carlo for QCD cascades in the color dipole formulation. LU-TP-88-5 (1988)
- [35] L. Lönnblad and U. Pettersson, ARIADNE 2: A Monte Carlo for QCD cascades in the color dipole formulation. LU-TP-88-15 (1988)
- [36] L. Lönnblad, ARIADNE 3: A Monte Carlo for QCD cascades in the color dipole formulation. LU-TP-89-10 (1989)
- [37] L. Lönnblad, ARIADNE version 4: A Program for simulation of QCD cascades implementing the color dipole model. *Comput. Phys. Commun.* **71**, 15 (1992)
- [38] CTEQ Collaboration, H.L. Lai et al., Global QCD analysis of parton structure of the nucleon: CTEQ5 parton distributions. *Eur. Phys. J. C* **12**, 375 (2000).
[arXiv:hep-ph/9903282](https://arxiv.org/abs/hep-ph/9903282)
- [39] R. Brun et al., GEANT3. CERN-DD-EE-84-1
- [40] M. Schreck, Vacuum Cherenkov radiation for Lorentz-violating fermions. *Phys. Rev. D* **96**, 095026 (2017). [arXiv:1702.03171](https://arxiv.org/abs/1702.03171)
- [41] V.A. Kostelecký and A.J. Vargas, Lorentz and CPT tests with hydrogen, antihydrogen, and related systems. *Phys. Rev. D* **92**, 056002 (2015).
[arXiv:1506.01706](https://arxiv.org/abs/1506.01706)

Coefficient	Lower	Upper
c_u^{TX}	-2.5×10^{-4}	6.6×10^{-5}
c_u^{TY}	-1.7×10^{-4}	9.8×10^{-5}
c_u^{XY}	-3.2×10^{-4}	4.1×10^{-5}
c_u^{XZ}	-5.4×10^{-4}	1.4×10^{-4}
c_u^{YZ}	-3.7×10^{-4}	2.1×10^{-4}
$c_u^{XX} - c_u^{YY}$	-2.1×10^{-4}	2.5×10^{-4}
c_d^{TX}	-7.8×10^{-4}	2.0×10^{-4}
c_d^{TY}	-5.2×10^{-4}	3.0×10^{-4}
c_d^{XY}	-1.6×10^{-3}	2.0×10^{-4}
c_d^{XZ}	-2.7×10^{-3}	7.0×10^{-4}
c_d^{YZ}	-1.8×10^{-3}	1.0×10^{-3}
$c_d^{XX} - c_d^{YY}$	-1.0×10^{-3}	1.2×10^{-3}
c_s^{TX}	-9.6×10^{-4}	2.5×10^{-4}
c_s^{TY}	-6.4×10^{-4}	3.7×10^{-4}
c_s^{XY}	-2.6×10^{-3}	3.3×10^{-4}
c_s^{XZ}	-4.4×10^{-3}	1.2×10^{-3}
c_s^{YZ}	-3.0×10^{-3}	1.7×10^{-3}
$c_s^{XX} - c_s^{YY}$	-1.7×10^{-3}	2.0×10^{-3}

Table 1: Lower (upper) values of the c -type coefficients below (above) which the p -values for the χ^2 GOF test are smaller than 0.05.

Coefficient	Lower (GeV ⁻¹)	Upper (GeV ⁻¹)
$a_{S_u}^{(5)TXX} - a_{S_u}^{(5)TYY}$	-5.1×10^{-7}	4.3×10^{-7}
$a_{S_u}^{(5)XXZ} - a_{S_u}^{(5)YYZ}$	-1.7×10^{-6}	2.0×10^{-6}
$a_{S_u}^{(5)TXY}$	-8.3×10^{-8}	6.5×10^{-7}
$a_{S_u}^{(5)TXZ}$	-2.9×10^{-7}	1.1×10^{-6}
$a_{S_u}^{(5)TYZ}$	-4.3×10^{-7}	7.4×10^{-7}
$a_{S_u}^{(5)XXX}$	-3.9×10^{-7}	1.2×10^{-7}
$a_{S_u}^{(5)XXY}$	-2.3×10^{-7}	1.8×10^{-7}
$a_{S_u}^{(5)XYY}$	-4.6×10^{-7}	9.2×10^{-8}
$a_{S_u}^{(5)XYZ}$	-2.6×10^{-6}	3.3×10^{-7}
$a_{S_u}^{(5)XZZ}$	-5.4×10^{-7}	1.4×10^{-7}
$a_{S_u}^{(5)YYY}$	-2.9×10^{-7}	1.5×10^{-7}
$a_{S_u}^{(5)YZZ}$	-3.6×10^{-7}	2.1×10^{-7}
$a_{S_d}^{(5)TXX} - a_{S_d}^{(5)TYY}$	-7.3×10^{-6}	6.1×10^{-6}
$a_{S_d}^{(5)XXZ} - a_{S_d}^{(5)YYZ}$	-2.4×10^{-5}	2.8×10^{-5}
$a_{S_d}^{(5)TXY}$	-1.2×10^{-6}	9.4×10^{-6}
$a_{S_d}^{(5)TXZ}$	-4.1×10^{-6}	1.6×10^{-5}
$a_{S_d}^{(5)TYZ}$	-6.1×10^{-6}	1.1×10^{-5}
$a_{S_d}^{(5)XXX}$	-5.7×10^{-6}	1.7×10^{-6}
$a_{S_d}^{(5)XXY}$	-3.4×10^{-6}	2.7×10^{-6}
$a_{S_d}^{(5)XYY}$	-6.8×10^{-6}	1.3×10^{-6}
$a_{S_d}^{(5)XYZ}$	-3.7×10^{-5}	4.6×10^{-6}
$a_{S_d}^{(5)XZZ}$	-8.1×10^{-6}	2.1×10^{-6}
$a_{S_d}^{(5)YYY}$	-4.3×10^{-6}	2.3×10^{-6}
$a_{S_d}^{(5)YZZ}$	-5.4×10^{-6}	3.1×10^{-6}

Table 2: Lower (upper) values of the $a^{(5)}$ -type coefficients below (above) which the p -values for the χ^2 GOF test are smaller than 0.05.

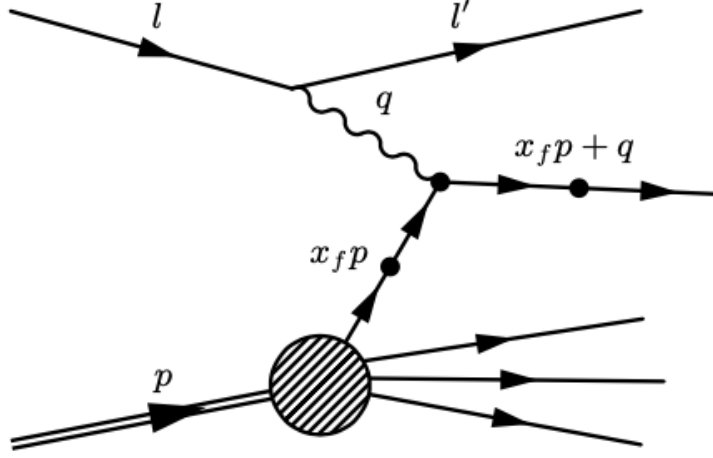


Figure 1: Parton-model picture of deep inelastic scattering with Lorentz violation. The dots on the incident parton, struck parton, and at the photon-parton vertex correspond to modified propagation and interaction due to Lorentz violation. The parton carries a momentum fraction x_f that is perturbed from x_{Bj} by the coefficients for Lorentz violation at first order.

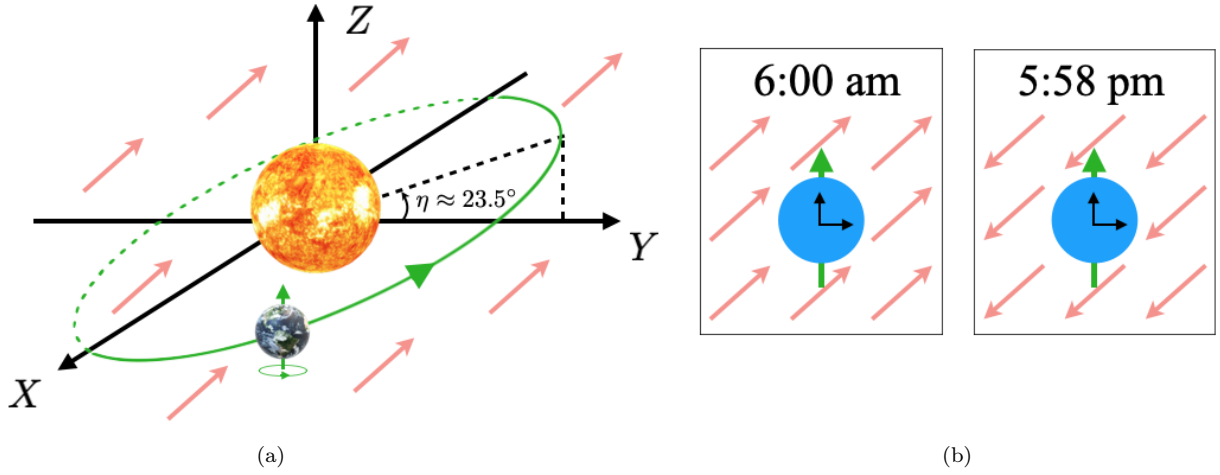


Figure 2: Sun-centred frame (SCF) (a). The orbit of the Earth in the SCF is shown in green. As the Z axis is parallel to the Earth's rotation axis, the orbit is inclined by the angle η . The effect of Lorentz violation is depicted as red background arrows. A laboratory on Earth studying a particle with spin (blue disk and green arrow) with coordinates given by black arrows centred on the particle will observe background configurations as a function of the sidereal period $T_{\text{sidereal}} \approx 23 \text{ h } 56 \text{ min}$ (b). The times depicted are an illustration of the sidereal effect.

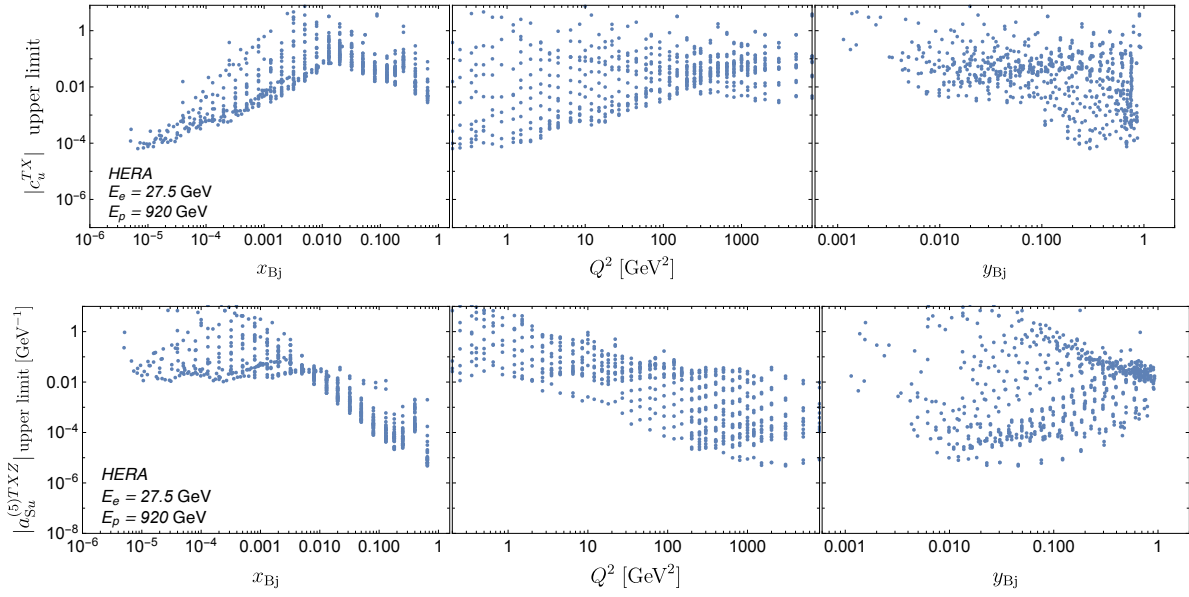


Figure 3: Regions in x_{Bj} , Q^2 and y_{Bj} that have sensitivity to Lorentz-violating effects for a single c -type and a $a^{(5)}$ -type coefficient. The points displayed in the plots are taken from Figures 2 and 4 of Ref. [9], where no experimental restrictions on the kinematic region have been considered.

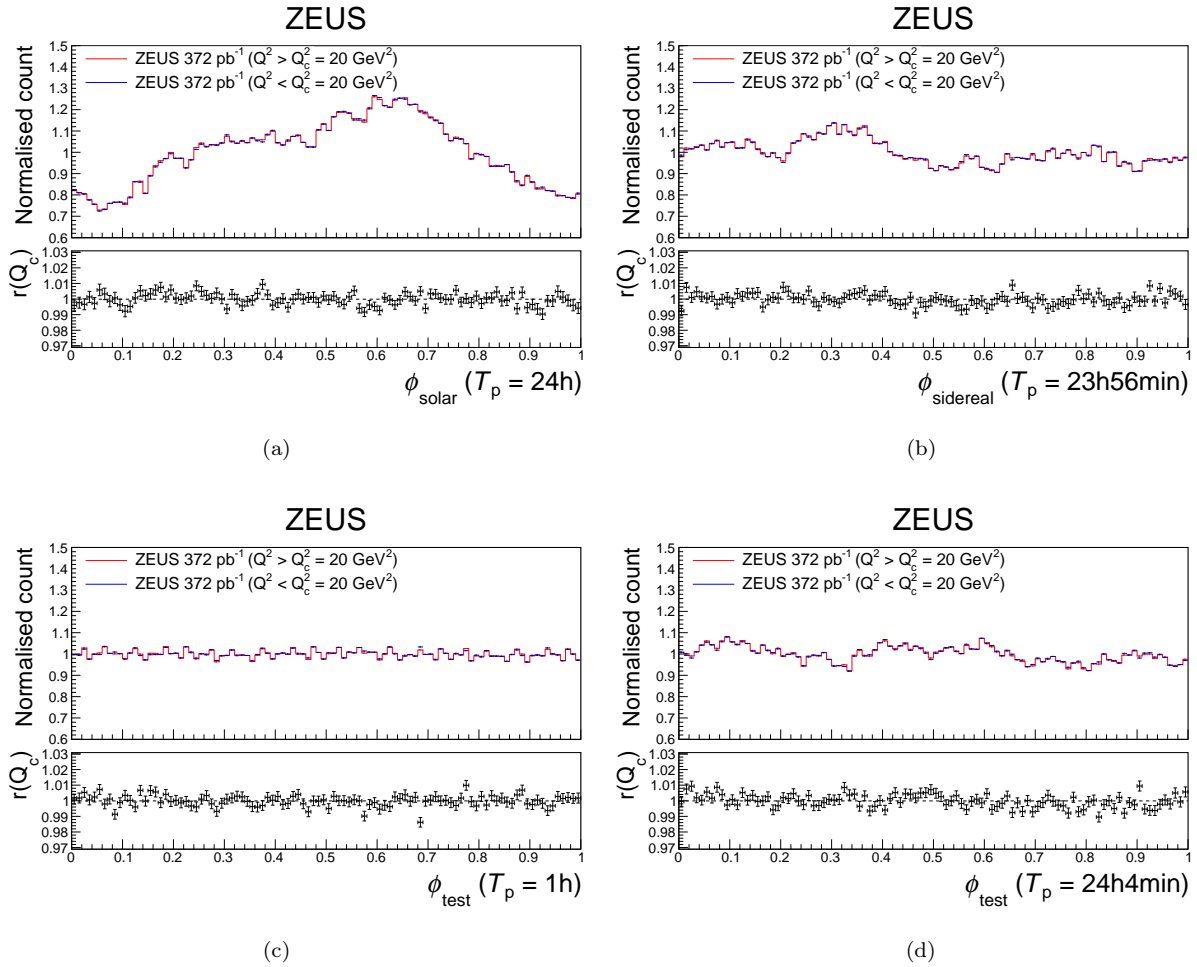


Figure 4: Solar (a), sidereal (b), $T_p = 1$ h (c) and $T_p = 24$ h 4 min (d) phase dependence of the normalised counts in 100 bins with the kinematic region divided by $Q_c^2 = 20$ GeV². The vertical axis displays the number of events per bin normalised to the total number of events times the bin width. The ratios of the counts $r(Q_c)$ above and below Q_c^2 are given in the bottom panels. For the solar phase, $\phi_{\text{solar}} = 0$ is identified with 11:20 UTC. Only statistical uncertainties are displayed.

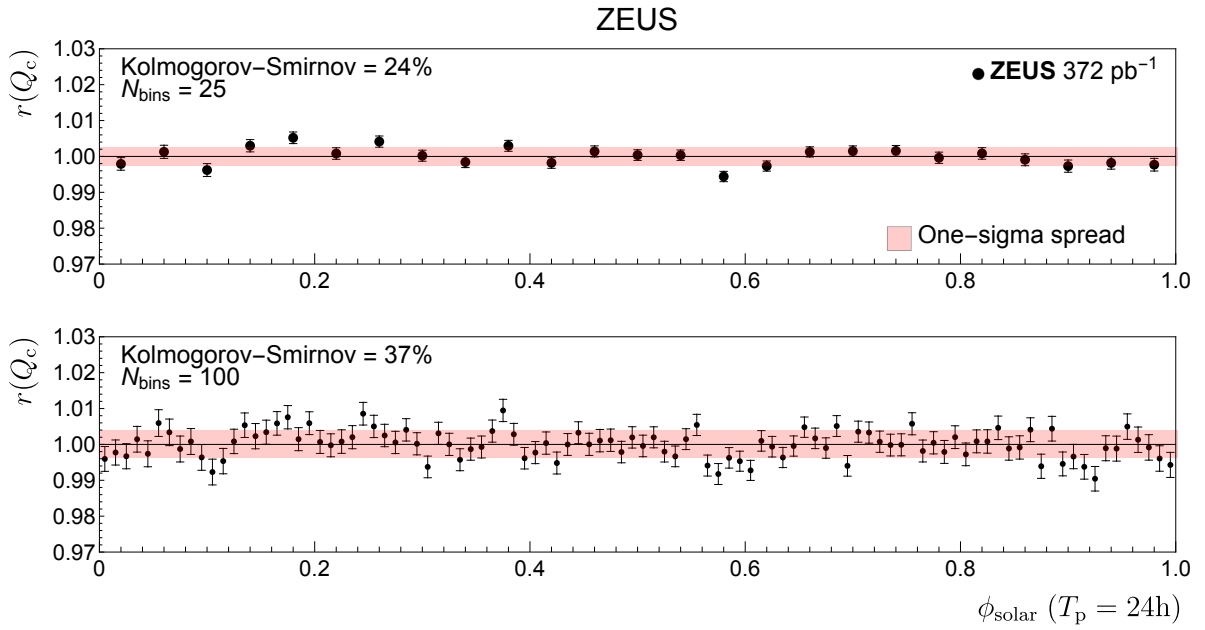


Figure 5: Ratio $r(Q_c)$ of normalised counts for $Q_c^2 = 20 \text{ GeV}^2$ binned with the solar phase where $N_{\text{bins}} = 25$ and 100. The case $N_{\text{bins}} = 100$ from Fig. 4(a) is repeated. The displayed uncertainties include statistical uncertainties only and the one-sigma spreads (bands) are the standard deviations of the central values. The observed distributions are compared to a Gaussian distribution in which only statistical errors are included using a Kolmogorov-Smirnov test.

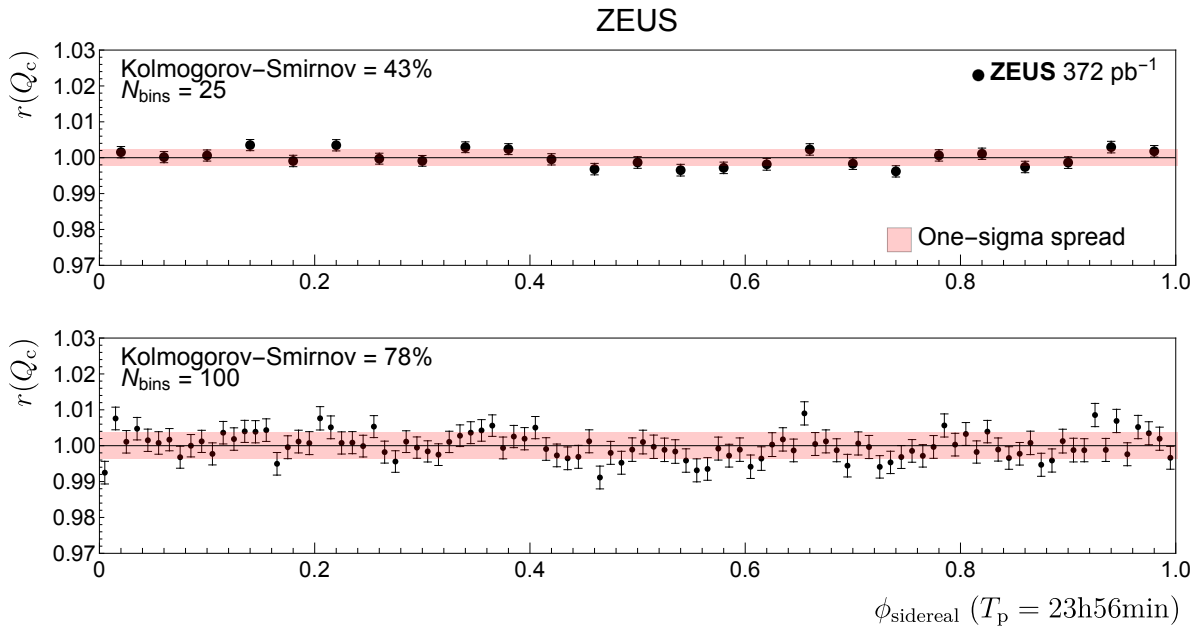


Figure 6: Ratio $r(Q_c)$ of normalised counts for $Q_c^2 = 20 \text{ GeV}^2$ binned with the sidereal phase where $N_{\text{bins}} = 25$ and 100. The displayed uncertainties include statistical uncertainties only and the one-sigma spreads (bands) are the standard deviations of the central values. The observed distributions are compared to a Gaussian distribution in which only statistical errors are included using a Kolmogorov–Smirnov test.

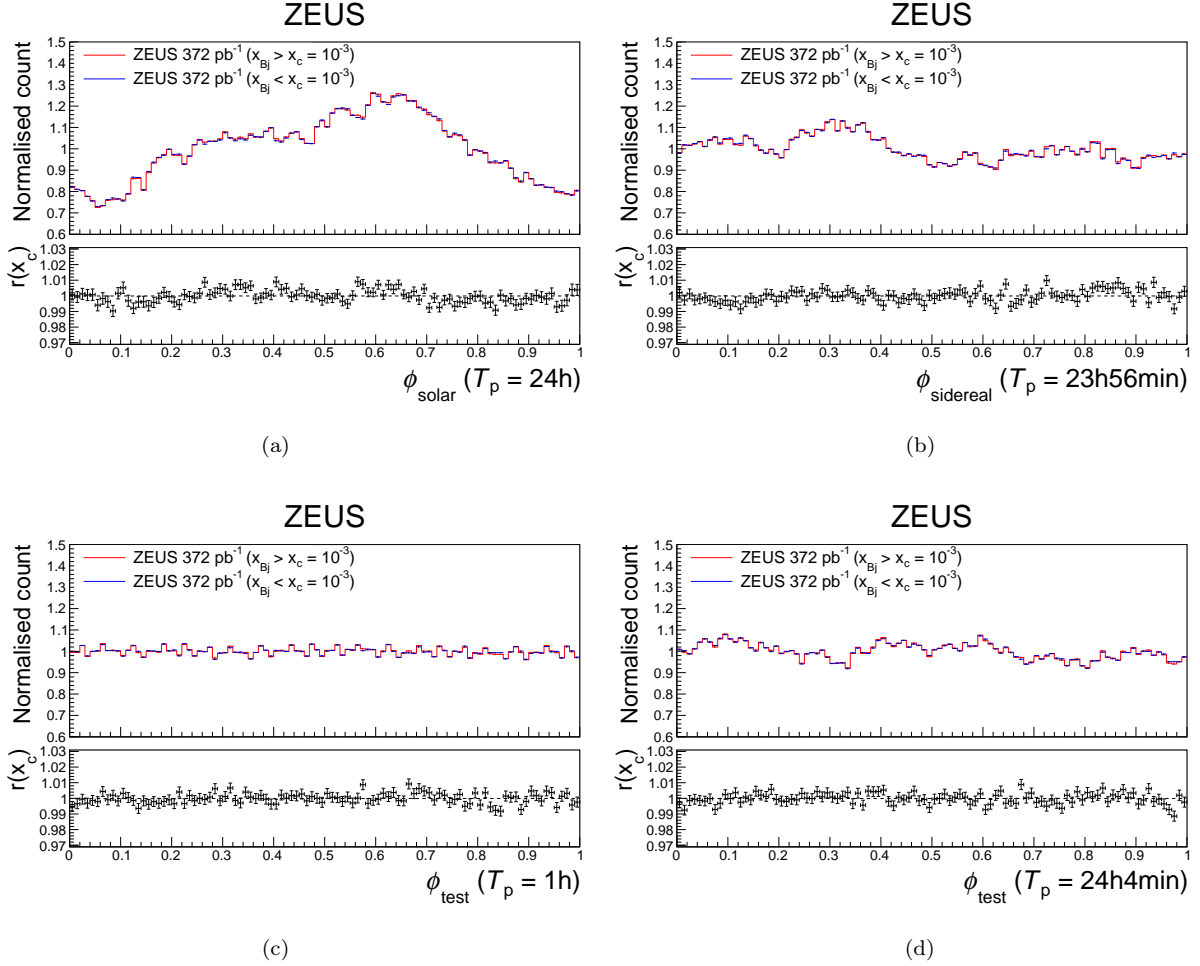


Figure 7: Solar (a), sidereal (b), $T_p = 1$ h (c) and $T_p = 24$ h 4 min (d) phase dependence of the normalised counts in 100 bins with the kinematic region divided by $x_c = 10^{-3}$. The vertical axis displays the number of events per bin normalised to the total number of events times the bin width. The ratios of the counts $r(x_c)$ above and below x_c are given in the bottom panels. For the solar phase, $\phi_{\text{solar}} = 0$ is identified with 11:20 UTC. Only statistical uncertainties are displayed.

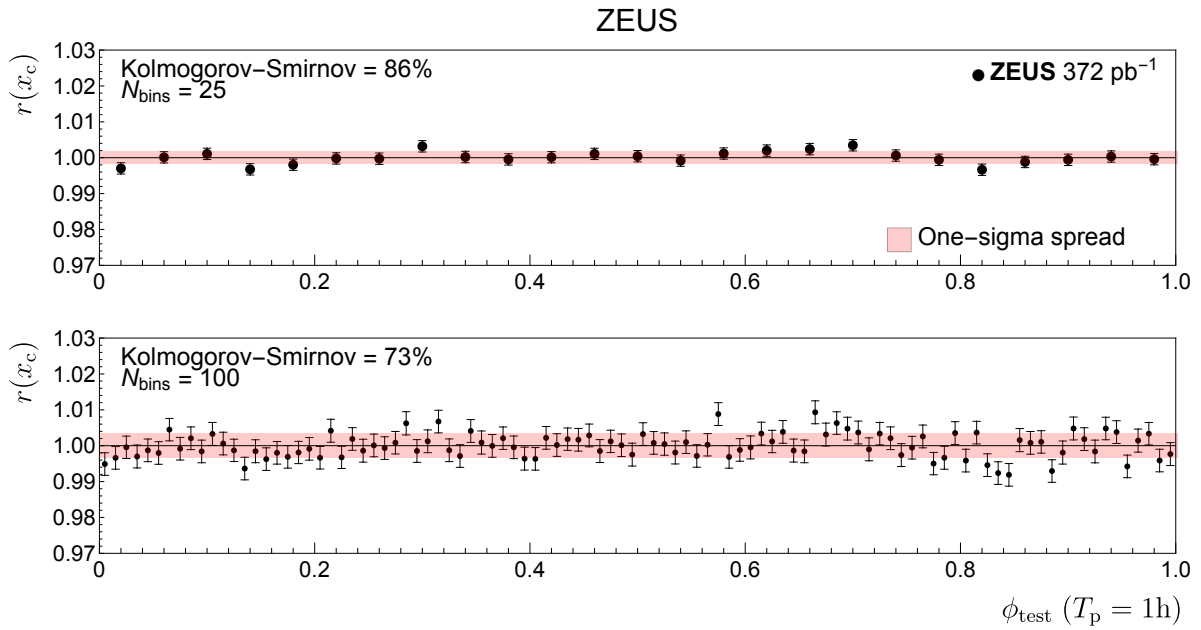


Figure 8: Ratio $r(x_c)$ of normalised counts for $x_c = 10^{-3}$ binned using the test phase with $T_p = 1$ h where $N_{\text{bins}} = 25$ and 100. The displayed uncertainties include statistical uncertainties only and the one-sigma spreads (bands) are the standard deviations of the central values. The observed distributions are compared to a Gaussian distribution in which only statistical errors are included using a Kolmogorov–Smirnov test.

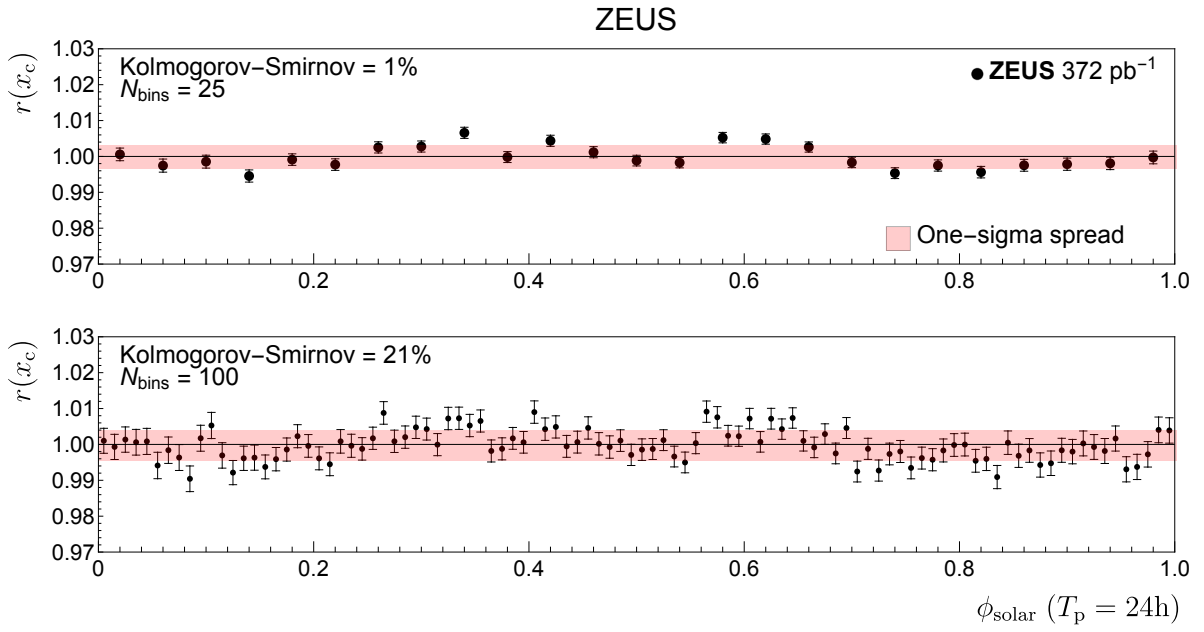


Figure 9: Ratio $r(x_c)$ of normalised counts for $x_c = 10^{-3}$ binned using the solar phase where $N_{\text{bins}} = 25$ and 100. The case $N_{\text{bins}} = 100$ from Fig. 7(a) is repeated. The displayed uncertainties include statistical uncertainties only and the one-sigma spreads (bands) are the standard deviations of the central values. The observed distributions are compared to a Gaussian distribution in which only statistical errors are included using a Kolmogorov-Smirnov test.

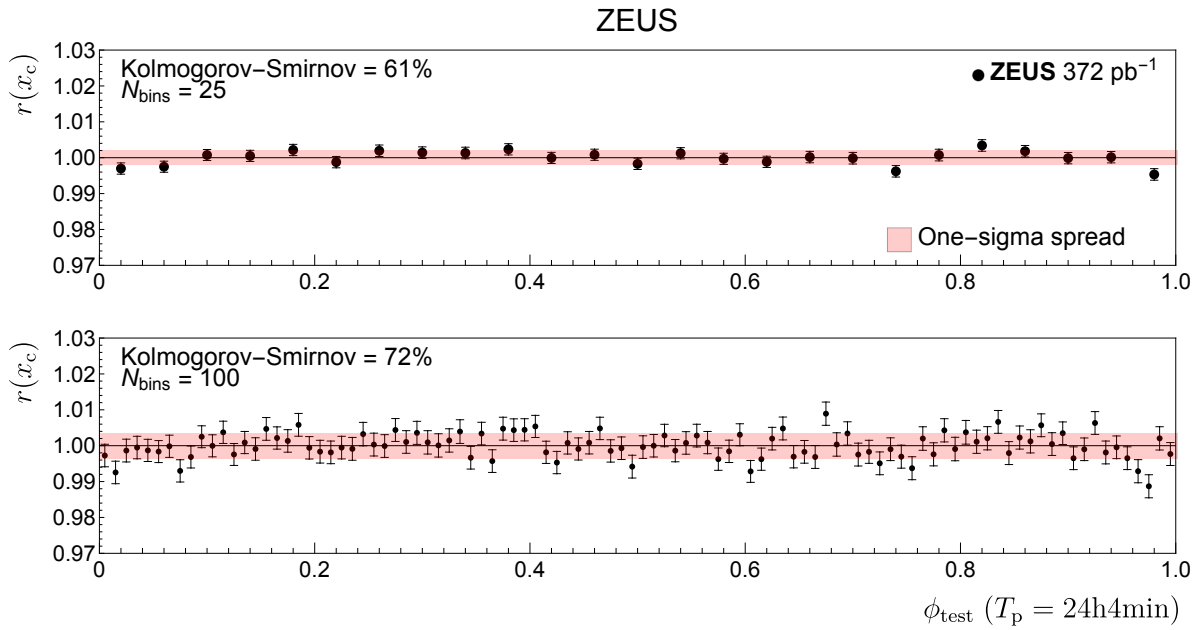


Figure 10: Ratio $r(x_c)$ of normalised counts for $x_c = 10^{-3}$ binned using the test phase with $T_p = 24$ h 4min where $N_{\text{bins}} = 25$ and 100. The displayed uncertainties include statistical uncertainties only and the one-sigma spreads (bands) are the standard deviations of the central values. The observed distributions are compared to a Gaussian distribution in which only statistical errors are included using a Kolmogorov–Smirnov test.

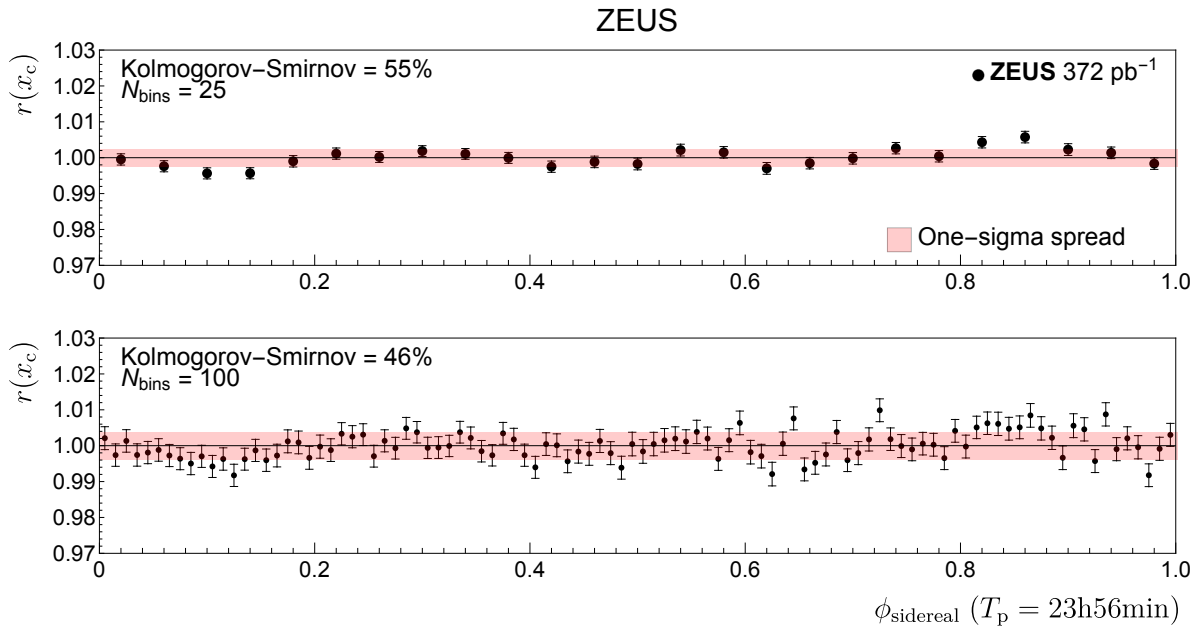


Figure 11: Ratio $r(x_c)$ of normalised counts for $x_c = 10^{-3}$ binned using the sidereal phase where $N_{\text{bins}} = 25$ and 100. The displayed uncertainties include statistical uncertainties only and the one-sigma spreads (bands) are the standard deviations of the central values. The observed distributions are compared to a Gaussian distribution in which only statistical errors are included using a Kolmogorov–Smirnov test.

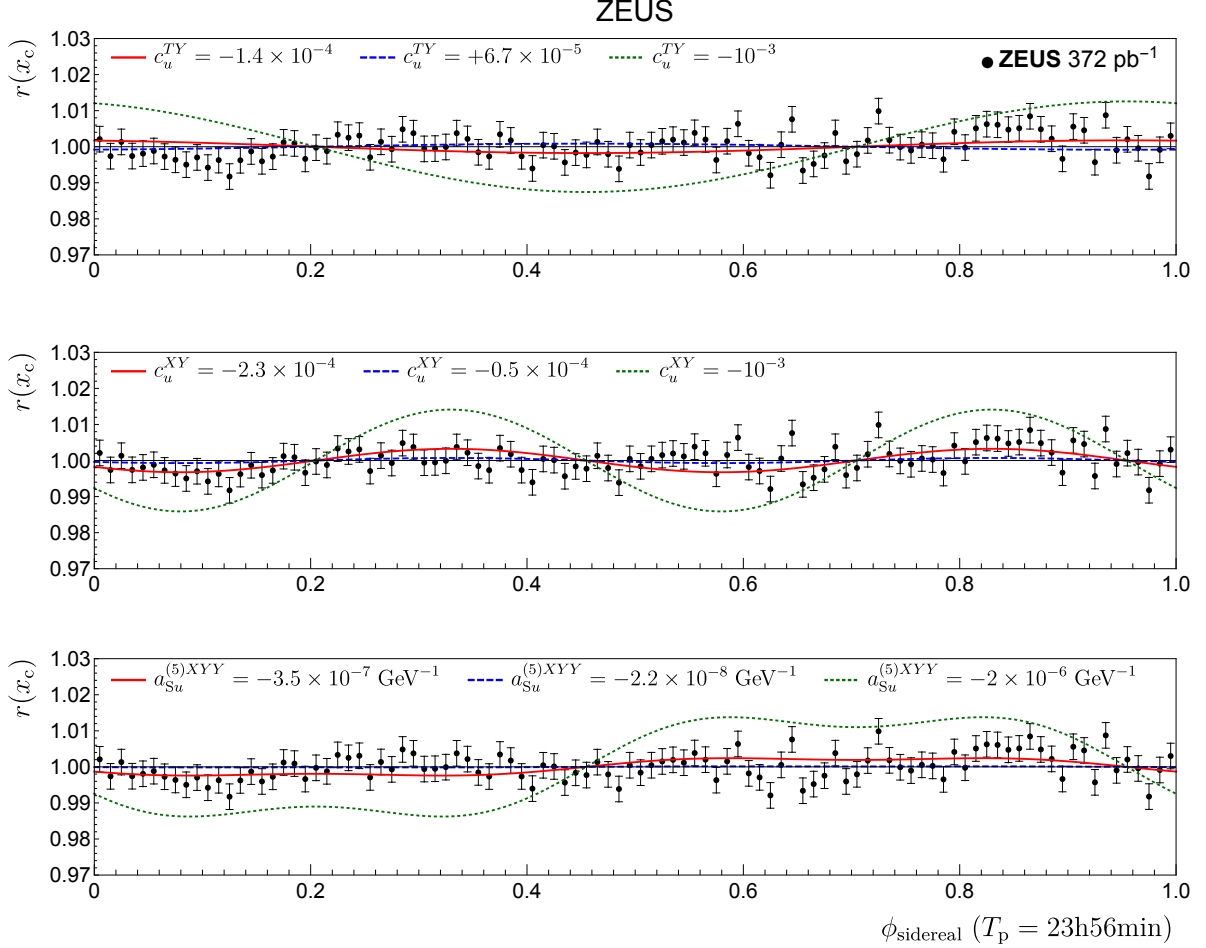


Figure 12: Ratio $r(x_c)$ of normalised counts for $x_c = 10^{-3}$ binned using the sidereal phase where $N_{\text{bins}} = 100$. The displayed uncertainties include statistical uncertainties only. In the three panels, signals corresponding to the SME coefficients c_u^{TY} , $c_u^{XX} - c_u^{YY}$ and $a_{\text{Su}}^{(5)XY}$ which are associated with variations up to ω_{\oplus} , $2\omega_{\oplus}$, and $3\omega_{\oplus}$, respectively, are displayed with values selected at the edge of the disfavoured ranges presented in Tables 1 and 2 (solid, dashed and dotted lines). In addition, signals that are excluded by the extracted bounds are displayed with $c_u^{TY} = 10^{-3}$, $c_u^{XX} - c_u^{YY} = 10^{-3}$, and $a_{\text{Su}}^{(5)XY} = +2 \times 10^{-6} \text{ GeV}^{-1}$.